Metallicities of Young Massive Clusters in NGC 5236 (M83)

Hernandez, Svea; Larsen, Søren; Trager, Scott; Kaper, Lex; Groot, Paul

Published in:
Monthly Notices of the Royal Astronomical Society

DOI:
10.1093/mnras/stx2397

Publication date:
2018

Monthly Notices
of the
ROYAL ASTRONOMICAL SOCIETY

MNRAS **473,** 826–837 (2018) doi:10.1093/mnras/stx2397
Advance Access publication 2017 September 15

Metallicities of young massive clusters in NGC 5236 (M83)

Svea Hernandez,[1]★ Søren Larsen,[1] Scott Trager,[2] Lex Kaper[3] and Paul Groot[1]

[1]*Department of Astrophysics/IMAPP, Radboud University, PO Box 9010, NL-6500 GL Nijmegen, the Netherlands*
[2]*Kapteyn Astronomical Institute, University of Groningen, Postbus 800, NL-9700 AV Groningen, the Netherlands*
[3]*Astronomical Institute Anton Pannekoek, Universiteit van Amsterdam, Postbus 94249, NL-1090 GE Amsterdam, the Netherlands*

Accepted 2017 September 12. Received 2017 September 11; in original form 2017 July 21

ABSTRACT

We present integrated-light (IL) spectra of eight young massive clusters (YMCs) in the metal-rich spiral galaxy NGC 5236 (M83). The observations were taken with the X-Shooter spectrograph on the ESO Very Large Telescope. Through the use of theoretical isochrones and synthetic IL spectra, we derive metallicities and study the radial metallicity gradient observed through these young populations. For the inner regions of the galaxy, we observe a relatively shallow metallicity gradient of -0.37 ± 0.29 dex R_{25}^{-1}, agreeing with chemical evolution models with an absence of infall material and a relatively low mass-loss due to winds in the inner parts of the disc. We estimate a central metallicity of $[Z] = +0.17 \pm 0.12$ dex, finding excellent agreement with that obtained via other methods (e.g. blue supergiants and *J* band). We infer a metallicity of $12+\log(\mathrm{O/H}) = 8.75 \pm 0.08$ dex at $R/R_{25} = 0.4$, which fits the stellar mass–metallicity relation compilation of blue supergiants and IL studies.

Key words: galaxies: abundances – galaxies: individual: NGC 5236.

1 INTRODUCTION

The study of stellar chemical abundances has proven to be a strong tool in constraining the star formation histories of different galaxies, particularly our own Milky Way (MW; Worthey 1998; Matteucci 2003; Venn et al. 2004; Pritzl, Venn & Irwin 2005). Knowledge of extragalactic chemical abundances is indispensable for understanding galaxy and chemical evolution on larger scales. Lequeux et al. (1979) and Tremonti et al. (2004), amongst others, found that there is a correlation between the mass and metallicity of individual galaxies. This mass–metallicity relation (MZR) has been used to learn about star formation episodes, galactic winds and general chemical enrichment of star-forming galaxies (Maiolino et al. 2008; Finlator & Davé 2008; Kudritzki et al. 2012; Lilly et al. 2013). Furthermore, radial metallicity variations within a galaxy provide valuable information on the effects of merging, initial mass function (IMF), infall and winds present in the galaxy (Prantzos & Boissier 2000; Sánchez-Blázquez et al. 2009; Kudritzki et al. 2015; Bresolin et al. 2016).

Studies of the chemical evolution of galaxies have been limited by the difficulty in obtaining reliable abundances and metallicities. Extragalactic metallicities of star-forming galaxies are generally measured using H II region emission lines. Two types of analyses predominate in this field: 'strong line' and 'T_e-based'. The former method is based on the ratio of fluxes from the strongest forbidden lines relative to Hβ (typically O; Pagel et al. 1979). On the other hand, the 'T_e-based' method uses auroral lines to infer the electron temperature of the gas. Even though these lines are weaker across a wide range of metallicities, this method removes the dependence on 'strong line' calibrations (Rubin et al. 1994; Lee, Salzer & Melbourne 2004; Stasińska 2005; Andrews & Martini 2013). One complication with this 'T_e-based' method occurs at metallicities close to solar and above, a regime where the auroral lines are extinguished (Stasińska 2005; Bresolin et al. 2005; Ercolano,Wesson & Bastian 2010; Zurita & Bresolin 2012). A well-known problem with these two methods comes to light by comparing the metallicities inferred from the different diagnostics. Studies have observed that different methods yield obvious systematic offsets in the inferred metallicities (Kennicutt et al. 2003; Kewley & Ellison 2008; Moustakas et al. 2010; López-Sánchez et al. 2012). However, even with its metallicity range limitations, Stasińska (2005) predicts that the 'T_e-based' method provides more robust measurements below solar metallicities.

In the last decade, spectroscopic observations of both red (RSG) and blue (BSG) supergiants have become an important tool to study the metallicities of extragalactic populations. The supergiant technique has been used as an alternative method for measuring metallicities and abundance gradients beyond the MW and even the Local Group (Bresolin et al. 2006, 2016; Evans et al. 2007; Davies, Kudritzki & Figer 2010; Kudritzki et al. 2013; Gazak et al. 2014b; Lardo et al. 2015; Kudritzki et al. 2016). Results from this technique show excellent agreement with abundances obtained from the 'T_e-based' method (Kudritzki et al. 2012, 2013, 2014; Hosek et al. 2014; Gazak et al. 2015).

★ E-mail: s.hernandez@astro.ru.nl

Table 1. X-Shooter observations.

Cluster	RA (J2000)	DEC (J2000)	t_{exp} (s) UVB	t_{exp} (s) VIS	S/N (pix^{-1}) UVB	S/N (pix^{-1}) VIS	Seeing (arcsec)
NGC 5236-245	204.248 735	−29.913 19	2000.0	1980.0	12.0	10.6	1.0
NGC 5236-254	204.167 693	−29.913 52	2000.0	1980.0	17.0	15.4	0.8
NGC 5236-367	204.261 056	−29.899 77	2000.0	1980.0	16.5	13.8	0.7
NGC 5236-805	204.258 142	−29.869 66	1620.0	1600.0	53.4	33.4	0.6
NGC 5236-1182	204.255 822	−29.846 55	2000.0	1980.0	58.5	35.4	0.7
NGC 5236-1234	204.270 055	−29.843 29	2000.0	1980.0	26.8	14.8	0.6
NGC 5236-1389	204.228 690	−29.832 62	2000.0	1980.0	27.8	17.1	0.6
NGC 5236-1471	204.236 777	−29.826 24	2000.0	1980.0	18.2	14.9	0.9

In addition to spectroscopic observations of H II regions and supergiants, other studies have developed techniques to obtain detailed abundances from high resolution ($R \sim 25\,000$) spectroscopic observations of unresolved extragalactic globular clusters (GC; McWilliam & Bernstein 2002, 2008; Bernstein & McWilliam 2005; Colucci et al. 2009, 2011, 2012; Larsen et al. 2012, 2014). With similar masses as GCs ($>10^4\,M_\odot$), young massive clusters (YMCs) are characterized by their young ages (<100 Myr; Portegies Zwart, McMillan & Gieles 2010). The identification of significant populations of YMCs in galaxies with on-going star formation (Larsen & Richtler 1999; Larsen 2004) has allowed the study of star formation histories and chemical evolution of individual galaxies to expand its parameter space. It is now feasible to learn about the recent chemical evolution of the stellar components in extragalactic environments. In Hernandez et al. (2017), we demonstrate that detailed abundance analysis is possible for intermediate-resolution observations ($R<$ 8800) of YMCs using NGC 1313 (∼4 Mpc) and NGC 1705 (∼5 Mpc) as test cases applying the spectral synthesis technique. Furthermore, the *J*-band method was recently used to measure accurate metallicities of extragalactic YMCs (Gazak et al. 2014a,b; Lardo et al. 2015). An additional advantage of studying the chemical histories of galaxies using star clusters (GCs/YMCs) over H II regions is the fact that H II regions trace the present-day metallicity of the gas phase, while star clusters can provide information on a broad range of ages/times. This paper aims to further exploit the recently developed techniques for integrated-light (IL) studies by exploring higher metallicity environments (above solar), such as those observed in the spiral galaxy NGC 5236 (M83; Bresolin & Kennicutt 2002; Bresolin et al. 2005) located at a distance of 4.9 Mpc (Jacobs et al. 2009).

In this work, we present the analysis of intermediate-resolution IL observations of eight YMCs distributed throughout NGC 5236 in an effort to determine the metallicity gradient across the disc of the galaxy. In Section 2, we provide a brief description of the X-Shooter spectrograph, target selection and science observations, followed by details on our data reduction approach. In Section 3, we present the abundance analysis applied in this work where we include information on the atmospheric models, stellar parameters and creation of the synthetic observations. We introduce our main results in Section 4 followed by our discussion in Section 5. We summarize our main remarks in Section 6.

2 OBSERVATIONS AND DATA REDUCTION

2.1 Instrument, target selection and science observations

The data analysed here were taken with the X-Shooter spectrograph on ESO's Very Large Telescope (VLT), located on Cerro Paranal, Chile (Vernet et al. 2011). The instrument has a wavelength coverage between 3000 and 24 800 Å. This broad coverage is possible due to its three-arm system, UV-blue (UVB), visible (VIS), and near-IR (NIR). Depending on the configuration the spectrograph observes at resolutions ranging from $R = 3000$ to 17 000. The science exposures use slit widths 1.0 arcsec, 0.9 arcsec and 0.9 arcsec providing resolutions of $R \sim 5100$, 8800 and 5100 for the UVB, VIS and NIR arms, respectively. The data were collected using the standard nodding mode with an ABBA sequence under GTO programme 085.B-0111A in 2010 April. Telluric standard stars were observed as part of the GTO programme. Flux standard star observations were collected through the ESO X-Shooter calibration programme and downloaded from the archive to be used in the reduction of the science exposures. Due to the low signal to noise (S/N) in the NIR exposures, this work makes use of the science observations obtained with the UVB and VIS arms only. In Table 1, we list the different cluster IDs, coordinates, exposure times, S/N values for the corresponding arms and the seeing.

The YMCs were selected using the catalogue by Larsen (2004). The selection criteria required uncontaminated objects and magnitudes brighter than $V = 19$. In Fig. 1, we show the location of the individual YMCs in NGC 5236 analysed in this work.

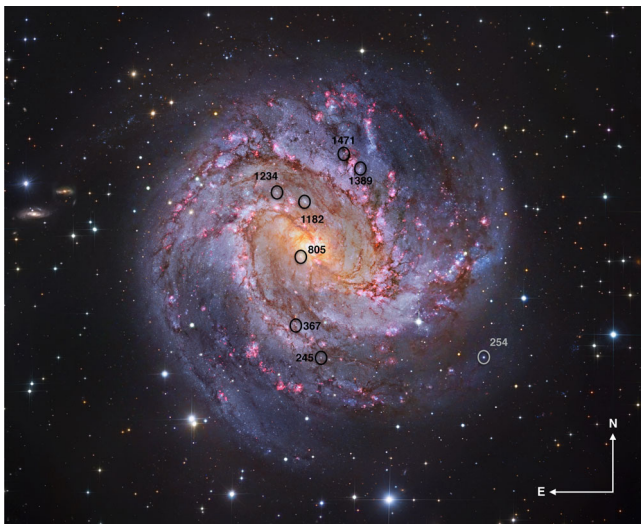

Figure 1. A colour-composite image of NGC 5236 observed with the 8.2-metre Subaru Telescope (NAOJ), the 2.2-metre Max Planck-ESO telescope and the *Hubble Space Telescope*. We mark the location of the different YMCs studied as part of this work. Image Credit: Subaru Telescope (NAOJ), *Hubble Space Telescope* and European Southern Observatory. Processing and Copyright: Robert Gendler.

2.2 Data reduction

The basic reduction steps are performed using the standard ESO Recipe Execution Tool (ESOREX) v3.11.1 and the public release of the X-Shooter pipeline v2.5.2. The spectral extraction is done using the IDL algorithms developed by Chen et al. (2014).

We flux calibrate the data using exposures of Feige 110, a spectrophotometric standard object observed close in time to the science data. For a more detailed discussion on the individual steps involved in the flux and telluric corrections, we point the reader to Hernandez et al. (2017). Briefly summarized, we create response curves for each of the science frames where we correct for exposure time and atmospheric extinction. For these response curves, we use the same flat-field and master bias frames applied to the corresponding science exposures. The telluric corrections for the VIS exposures are done using the telluric library compiled by the X-Shooter Spectral Library team along with a principal component analysis (PCA) routine created by Chen et al. (2014). This PCA algorithm removes and reconstructs the strongest telluric absorptions.

3 ABUNDANCE ANALYSIS

We make use of the analysis method developed by Larsen et al. (2012, hereafter L12) to obtain detailed abundances from IL observations of star clusters. The L12 method was originally designed and tested using high-dispersion ($R \sim 40\ 000$) spectroscopic observations, and extended to intermediate-resolution ($R < 8800$) observations by Hernandez et al. (2017).

Briefly summarized, we create a series of high-resolution ($R \sim 500\,000$) simple stellar population models where we include every evolutionary stage present in the star cluster. First, a series of atmospheric models is created using ATLAS9 (Kurucz 1970) and MARCS (Gustafsson et al. 2008). The former are used for stars with $T_{\rm eff} > 5000$ K, and the latter for $T_{\rm eff} < 5000$ K. Synthetic spectra for individual stars are created using SYNTHE (Kurucz & Furenlid 1979; Kurucz & Avrett 1981) and TURBOSPECTRUM (Plez 2012) for ATLAS9 and MARCS models, respectively. The spectra are then co-added to generate a synthetic IL spectrum for the star cluster in question. The synthetic spectra are then compared to the X-Shooter observations and the abundances are modified until the best match (minimum χ^2) between model and observations is obtained.

In this work, we make use of a scaling parameter relative to solar composition and apply it to all of the specified abundances. We note that the metallicity [Z] derived from this analysis is a measure of the integrated abundances of different chemical elements, including, and not limited to, α- and Fe-peak elements. The current software uses solar composition from Grevesse & Sauval (1998). Additionally, the code allows the user to assign weights to different parts of the spectrum on a pixel-to-pixel basis, with values ranging from 0.0 (exclusion) to 1.0 (inclusion). For our analysis, we set the weights to 0.0 in regions affected by instrumental features, telluric contamination and nebular/ISM emission.

3.1 Stellar parameters

We create a Hertzsprung–Russell diagram (HRD) to cover and represent every evolutionary stage in the YMC using the theoretical models from PARSEC v.1.2S (Bressan et al. 2012). Previous studies have found the metallicity of the disc of NGC 5236 to be above solar (Bresolin & Kennicutt 2002). For the initial selection of the isochrones, we adopt a metallicity [Z] = 0.3 and YMC ages found in the literature. The cluster ages have been estimated from photometric observations and applying the S-sequence age calibration defined by Girardi et al. (1995). This method relies on an age sequence derived from fitting the average colours of bright Large Magellanic Cloud (LMC) star clusters in the $U-B$ versus $B-V$ space and has been applied to star clusters external to the LMC (Bresolin, Kennicutt & Stetson 1996). Typical errors on these photometric ages are a factor of 2. In Table 2, we show the YMC properties, including the ages, masses, normalized galactocentric distance and effective radii, along with their corresponding literature reference.

Table 2. YMC properties. References for each of the clusters are listed as footnotes.

Cluster	log(age)	$\rm Mass_{phot}$ ($\rm M_\odot$)	R/R_{25}	$R_{\rm eff}$ (pc)
NGC 5236-245[a]	8.00	1.4×10^5	0.44	5.4
NGC 5236-254[b]	8.25	2.7×10^5	0.91	10.1
NGC 5236-367[a]	7.85	1.1×10^5	0.32	4.7
NGC 5236-805[c]	7.10	2.0×10^5	0.05	2.3
NGC 5236-1182[d]	7.45	2.1×10^5	0.17	6.8
NGC 5236-1234[d]	7.45	8.1×10^4	0.26	7.2
NGC 5236-1389[e]	7.69	1.1×10^4	0.39	8.7
NGC 5236-1471[a]	7.76	8.7×10^4	0.40	2.9

[a]Larsen (2004, 2009); Bastian et al. (2013),
[b]Larsen & Richtler (2006),
[c]Larsen & Richtler (2004),
[d]Larsen et al. (2011),
[e]Larsen (1999).

The stellar parameters ($T_{\rm eff}$, log g, M) are extracted from these theoretical isochrones assuming an IMF following a power law, $\mathrm{d}N/\mathrm{d}M \propto M^{-\alpha}$, adopting a Salpeter (1955) exponent of $\alpha = 2.35$, and a lower mass limit of 0.4 $\rm M_\odot$.

An additional feature in the L12 code is the capability to fit for the microturbulent velocity, $v_{\rm t}$. We initially fit for [Z] and $v_{\rm t}$ simultaneously for all eight YMCs. The code fits for a single $v_{\rm t}$ value and applies it to all the stars in the cluster, irrespective of type. We find a poorly constrained mean microturbulence of $\langle v_{\rm t} \rangle = 2 \pm 1$ km s^{-1}. Due to the large uncertainties in the calculated $v_{\rm t}$ we perform several tests changing the $v_{\rm t}$ from 1 to 2 km s^{-1} for stars with $T_{\rm eff} < 6000$ K. Changing the $v_{\rm t}$ values from 1 to 2 km s^{-1} changes the overall metallicity on average by $\lesssim$0.1 dex, with the exception of NGC 5236-1471 where [Z] changes by 0.19 dex. For the rest of our analysis, we adopt the following microturbulent values: $v_{\rm t} = 2$ km s^{-1} for stars with $T_{\rm eff} < 6000$ K, $v_{\rm t} = 4$ km s^{-1} for stars with $6000 < T_{\rm eff} < 22\,000$ K (Lyubimkov et al. 2004) and $v_{\rm t} = 8$ km s^{-1} for stars with $T_{\rm eff} > 22\,000$ K (Lyubimkov et al. 2004), similar to what was used in Hernandez et al. (2017).

3.2 Instrumental resolution and velocity dispersion

As mentioned before, we create a high-resolution ($R \sim 500\ 000$) model spectra that we degrade to match the resolution of our science observations. The L12 code has the option of fitting for the best Gaussian dispersion value ($\sigma_{\rm sm}$) used to smooth the model spectra. Using this feature, we fit for the best $\sigma_{\rm sm}$ and [Z] values, analysing 200 Å of data at a time. We repeat this procedure to obtain the $\sigma_{\rm sm}$ of each of the YMCs in our sample. In general, the $\sigma_{\rm sm}$ accounts for the finite instrumental resolution ($\sigma_{\rm inst}$) and the internal velocity dispersions in the cluster ($\sigma_{\rm 1D}$).

Chen et al. (2014) report that the X-Shooter resolution in the UVB arm varies with wavelength, but remains constant in the VIS arm. Following this same assumption and that where the resolving

Table 3. YMCs derived quantities.

Cluster	σ_{1D} (km s^{-1})	[Z] (dex)	σ_{err} (dex)	N	v_{rv} (km s^{-1})
NGC 5236-245	5.1 ± 2.4	+0.02	0.06	9	559 ± 5
NGC 5236-254	7.3 ± 6.9	−0.14	0.11	9	558 ± 32
NGC 5236-367	6.0 ± 1.7	+0.00	0.09	9	535 ± 5
NGC 5236-805	7.7 ± 4.4	+0.17	0.12	9	496 ± 4
NGC 5236-1182	8.0 ± 6.4	+0.17	0.13	9	461 ± 5
NGC 5236-1234	6.9 ± 4.8	+0.06	0.21	9	441 ± 4
NGC 5236-1389	7.1 ± 5.6	+0.04	0.09	9	472 ± 3
NGC 5236-1471	5.3 ± 2.3	+0.12	0.09	9	469 ± 2

power represents a Gaussian full width at half-maximum (FWHM), we use the same instrumental resolution as that presented in Hernandez et al. (2017), $\sigma_{inst} = 14.47\,km\,s^{-1}$. We estimate the cluster velocity dispersions using the average σ_{sm} calculated from the VIS observations alone. The line-of-sight velocity dispersion for each of the clusters is obtained through the following relation:

$$\sigma_{1D} = \sqrt{\sigma_{sm}^2 - \sigma_{inst}^2}. \quad (1)$$

Our analysis assumes an instrumental resolution set by the slit width alone. We note that the velocity dispersions may be underestimated if the actual resolution is higher than the standard instrumental resolution (e.g. if the seeing FWHM is smaller than the slit width). In Table 3, we summarize the derived line-of-sight velocity dispersions for the different YMCs included in this work. We note that for YMC NGC 5236-805 Larsen & Richtler (2004) infer a line-of-sight velocity dispersion of $\sigma_{1D} = 8.1 \pm 0.2\,km\,s^{-1}$, which is comparable to our measured velocity dispersion of $\sigma_{1D} = 7.7 \pm 4.4\,km\,s^{-1}$.

We take the σ_{1D} along with the effective radii listed in Table 2 and estimate the dynamical masses ($Mass_{dyn}$) using the following relation:

$$M_{dyn} = \alpha \frac{\sigma_{1D}^2 R_{eff}}{G}, \quad (2)$$

where $\alpha \sim 9.75$. The cluster masses listed in Table 2, $Mass_{phot}$, are estimated using the M/L models of Bruzual & Charlot using a Salpeter IMF. In Fig. 2, we show the $Mass_{phot}$ as a function of $Mass_{dyn}$. The dynamical masses appear to be slightly higher than the photometric masses; however, both are consistent within the large uncertainties.

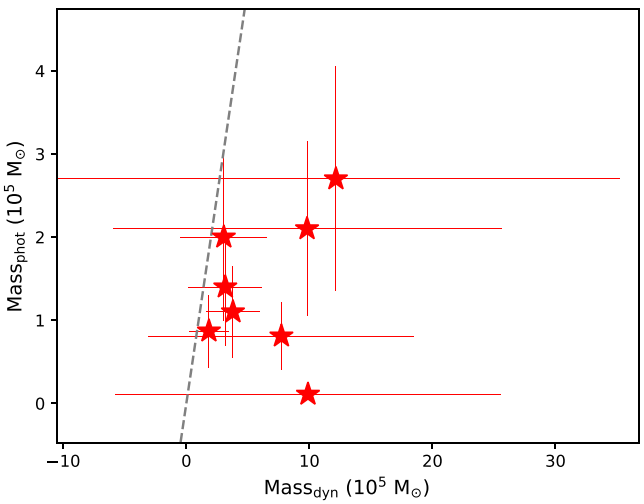

Figure 2. Photometric mass, $Mass_{phot}$ as a function of dynamical mass, $Mass_{don}$. We note that the errors on the photometric masses are a factor of 2 (Bastian et al. 2013). We show the line of equal value in grey.

4 RESULTS

After obtaining the best smoothing parameter (σ_{sm}), we proceed to estimate [Z], keeping σ_{sm} fixed. Similar to the analysis in Hernandez et al. (2017), we fit for the [Z] of each of the clusters scanning the UVB and VIS wavelengths using 200 Å bins, excluding telluric-contaminated bins and those affected by the noise near the edge of the arms (5200–5400 Å and 5400–5600 Å for the UVB and VIS arms, respectively). We use a cubic spline with three knots to match the model continua to the observed spectra. In Fig. 3, we show example synthesis fits for all the YMCs. The individual metallicity measurements obtained for the different wavelength bins and their corresponding 1σ uncertainties from the χ^2 fit are listed in Tables A1–A8 of the appendix. Once the minimum χ^2 (χ^2_{min}) has been found the 1σ uncertainties are estimated by varying the metallicity until $\chi^2 = \chi^2_{min} + 1$. We note that in our final bin consideration we exclude UVB wavelengths between 4400 and 5200 Å mainly because in every iteration when we change the input isochrone (different age and metallicity), the measured [Z] values for these wavelengths change drastically; this in contrast to the rest of the bins where the values remain relatively constant in spite of a change in input isochrone. These changes were in the order of ∼0.2–0.4 dex, depending on the cluster. This behaviour was observed in all YMCs. Given the broad wavelength coverage in X-Shooter data, the exclusion of these bins does not impact our analysis.

In Table 3, we present weighted averaged metallicities, their corresponding errors (σ_{err}), the number of bins (N) included in the analysis and the estimated radial velocities (v_{rv}). The σ_{err} is calculated using equation 5 of Hernandez et al. (2017), where we account for the number of individual measurements (N) when estimating the errors on the mean metallicities along with the weighted standard deviation,

$$\sigma_{STD} = \sqrt{\frac{\sum w_i (Z_i - \bar{Z}_w)^2}{\frac{N_{nonz}-1}{N_{nonz}} \sum w_i}}. \quad (3)$$

In equation (3), the individual weights are represented by w_i and defined as $w_i = 1/\sigma_i^2$, N_{nonz} is the number of non-zero weights, the different bin metallicities are identified as Z_i and the weighted average metallicities as $\bar{Z}_w$. This approach for σ_{err} is chosen given that the scatter in individual measurements is larger than the errors based on the χ^2 fitting; therefore, more representative of the actual uncertainties in the measurements.

In Hernandez et al. (2017), we observed that selecting an isochrone to self-consistently match the inferred metallicity for the youngest YMC with a log(age)= 7.1, NGC 1705-1, does not necessarily converge on the best model spectrum in spite of measuring similar metallicities (see fig. 7 in Hernandez et al. 2017). We note that the behaviour seen in NGC 1705-1 was not present in the analysis of the youngest cluster in this study or in any of the other YMCs. Using an initial isochrone of metallicity [Z] ∼+ 0.33 dex for NGC 5236-805, we estimate an overall metallicity of [Z] ∼+ 0.13 dex. We then continue our analysis changing the input isochrone metallicity to [Z] ∼+ 0.20 dex, and derive a final metallicity of [Z] ∼+ 0.17 dex. In contrast to NGC 1705-1, visually inspecting the individual fits shows that the best model spectra generated using the

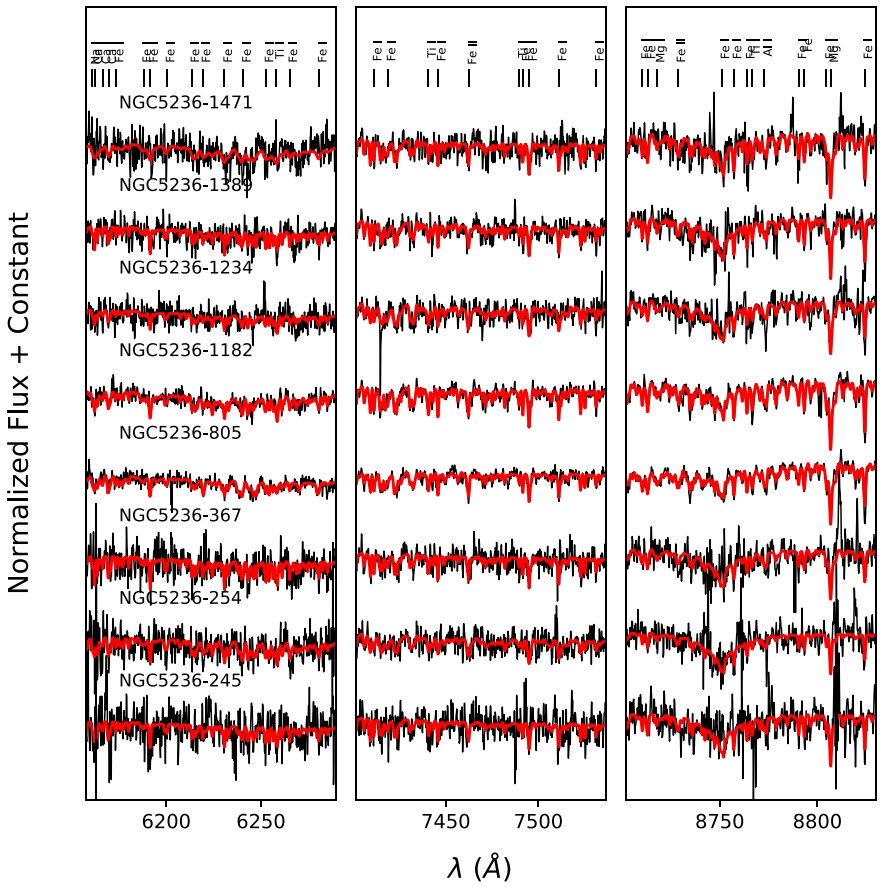

Figure 3. Normalized integrated spectra for individual observations (in black) with its corresponding best-fitting models (in red). We have added a constant offset for the benefit of visualization. The cluster IDs are shown.

isochrones with metallicity similar to the derived values match the observations well and decreases the final $\chi^2_{\rm red}$ values (see Fig. 4).

4.1 Sensitivity to ATLAS9/MARCS models and spectral synthesis computations

As described in Section 3, we use two different sets of models depending on the $T_{\rm eff}$ of the star. For cool stars ($T_{\rm eff} < 5000$ K), we use MARCS atmospheric models along with the TURBOSPECTRUM software to compute the synthetic spectra. The MARCS models allow for spherically symmetric stellar atmospheres, generally preferred for stars with extended atmospheres compared to the plane-parallel symmetry used in ATLAS9 models. In this work, we use a boundary in $T_{\rm eff}$ to separate the majority of giants from dwarfs. In Fig. 5, we show the final isochrones used for the different clusters. Displayed in red circles are those stars with $T_{\rm eff} < 5000$ K, mainly covering the giant-like types. We point out that some lower main-sequence stars are also identified to have $T_{\rm eff} < 5000$ K; however, their contribution to the IL spectrum is rather small. Stars with $T_{\rm eff} > 5000$ K are shown in black triangles. From Fig. 5, it is clear that a $T_{\rm eff}$ boundary of 5000 K reasonably covers the supergiant regime, located in the evolved branch of the HRD (red circles with $M_{\rm V} \sim -2.5$).

To explore how sensitive our metallicity measurements are to the different model choices, we compare the metallicities inferred using different $T_{\rm eff}$ boundaries. In the first run, we set a $T_{\rm eff}$ boundary of 3500 K. With this temperature boundary we use ATLAS9 models for the majority of the stars, including giants. The second run uses a boundary of $T_{\rm eff} = 5000$ K. Given the ages and metallicities of the

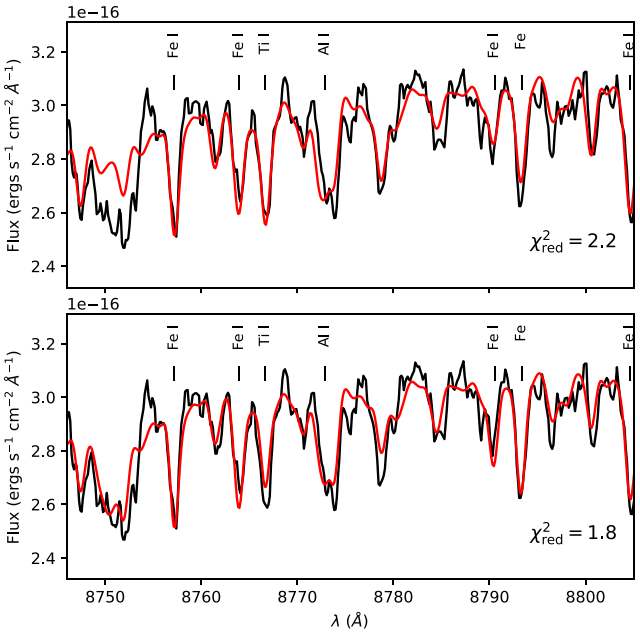

Figure 4. In black we show the X-Shooter observation of NGC 5236-805. Top: In red we show the best model spectrum for NGC 5236-805 generated with an isochrone of log(age) = 7.1 and $[Z] = +0.33$ dex. Bottom: In red we show the model spectrum for the same YMC using isochrone of log(age) = 7.1 and $[Z] = +0.20$ dex. We show the final $\chi^2_{\rm red}$ in the corresponding panels. See the text for details.

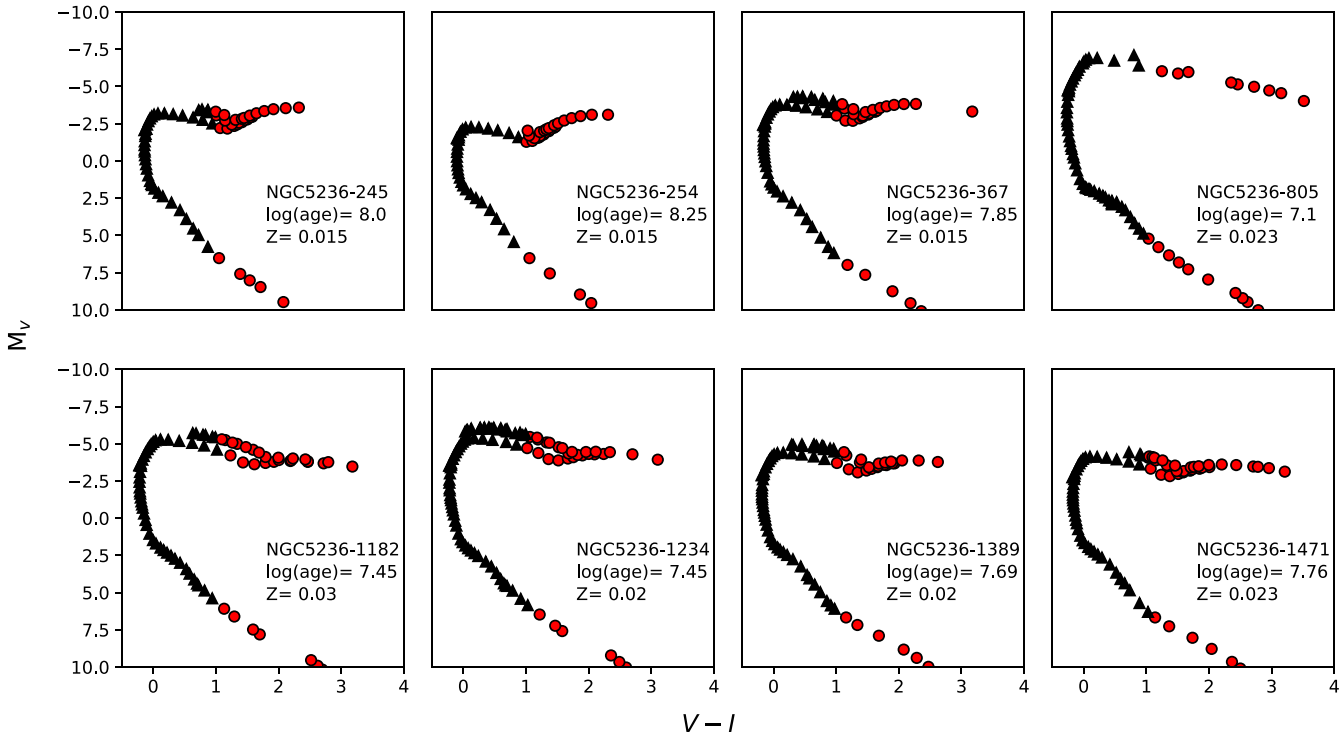

Figure 5. Theoretical isochrones corresponding to the best-fitting metallicities, *Z*, where $Z_{\odot} = 0.017$ (Grevesse & Sauval 1998). Using red circles we show stars with $T_{\rm eff} < 5000$ K, for which we use MARCS models. Using black triangles we show those stars with warmer temperatures ($T_{\rm eff} > 5000$ K) for which we used ATLAS9 models.

different clusters, the second run uses MARCS models for most of the giants (see Fig. 5). The results of this study are presented in the second column of Table 4. Changing the $T_{\rm eff}$ boundary from 3500 to 5000 K varies the inferred metallicity as much as 0.26 dex in the most extreme case. We note that in most cases this change in $T_{\rm eff}$ modifies the measured [*Z*] by <0.10 dex.

Given the intrinsic dependence of our analysis on the selection of theoretical models, we investigate how sensitive our results are to the input isochrone ages. We recalculate the metallicities of each of the clusters modifying the ages by a factor of 2. In the third column of Table 4, we show the results of this comparison. Changing the input ages by 2 × log (age), we see that the average metallicity change amongst all eight YMCs is ∼0.1 dex, with the highest metallicity change seen for NGC 5236-805 with a difference of $\Delta\,[Z] = -0.20$.

We point out that the work presented here is based solely on local thermodynamic equilibrium (LTE) models. At this moment, we do not correct for any non-LTE (NLTE) effects. Such corrections are dependent on the physical parameters of each individual star, which makes NLTE corrections particularly complicated for IL analysis. In the case of RSGs, studies have estimated NLTE corrections for [Fe/H] abundances of the order of ∼0.1 dex or lower (Bergemann et al. 2012). Higher NLTE corrections have also been predicted for some α-elements with values ranging from −0.4 to −0.1 dex (Bergemann et al. 2015).

Table 4. Sensitivity to ATLAS9/MARCS models.

Cluster	$\Delta\,T_{\rm eff}$ +1500 K	Δt 2 × log (age)
NGC 5236-245	−0.01	−0.12
NGC 5236-254	+0.09	−0.01
NGC 5236-367	−0.23	+0.02
NGC 5236-805	−0.09	+0.20
NGC 5236-1182	−0.01	+0.04
NGC 5236-1234	−0.26	−0.05
NGC 5236-1389	+0.15	−0.14
NGC 5236-1471	+0.08	+0.06

5 DISCUSSION

5.1 Mass–metallicity relation

The MZR is an important diagnostic tool in the inference of star formation scenarios, galactic winds and chemical histories of galaxies. As mentioned earlier, this relationship was observed in star-forming galaxies by Lequeux et al. (1979) through the study of H II regions in irregular and blue compact galaxies. Tremonti et al. (2004) and Andrews & Martini (2013) later expanded this study by analysing ∼53 000 and ∼200 000 star-forming galaxies and their gas-phase metallicity, respectively, further confirming the correlation between stellar mass and metallicity.

The MZR of star-forming galaxies has been studied exclusively through the analysis of nebular spectra. To compare the stellar and gaseous metallicity measurements, we plot our results in the mass–metallicity plane in Fig. 6. In this figure, we include the MZR inferred by Tremonti et al. (2004) and Andrews & Martini (2013) using the Sloan Digital Sky Survey, with dashed blue and solid green lines, respectively. Additionally, we include Kudritzki et al. (2016) compilation of metallicity measurements obtained through the BSG method as yellow circles and through the IL method from Hernandez et al. (2017) as red circles.

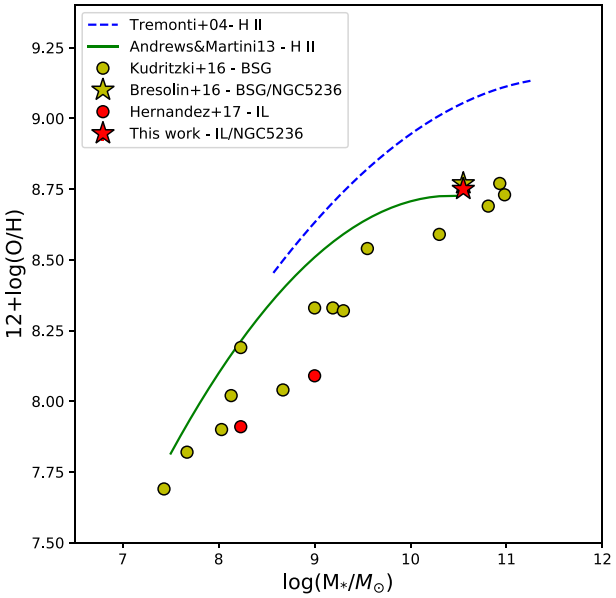

Figure 6. Mass–metallicity relation. The dashed blue line shows the polynomial fit determined by Tremonti et al. (2004). The solid green line displays the relation defined by Andrews & Martini (2013). The red star corresponds to the integrated metallicity for NGC 5236 obtained as part of this work. The yellow star shows the abundance estimated by Bresolin et al. (2016) for NGC 5236 using the BSG method. Yellow circles represent the stellar metallicities inferred by the BSG method, compiled by Kudritzki et al. (2016). Red circles represent the metallicities for NGC 1313 and NGC 1705 inferred by Hernandez et al. (2017).

We remark that our work measures the overall metallicity of the individual clusters, [*Z*]. In general, for spiral galaxies with metallicity gradients, one adopts a characteristic metallicity measured at $0.4R_{25}$. According to Zaritsky, Kennicutt & (1994) and Moustakas & Kennicutt (2006), metallicities of spiral galaxies at this radial distance from the centre coincides with the integrated metallicity of the whole galaxy. We note that while our spectral fit analysis uses Grevesse & Sauval (1998), in the following exercise we adopt the solar oxygen abundance of Asplund et al. (2009), 12+log (O/H) = 8.69. We average the metallicities measured for NGC 5236-1389, NGC 5236-1471 and NGC 5236-245 (all three YMCs located at $R \sim 0.4\ R_{25}$) and infer an average oxygen abundance of 12+log(O/H) = 8.75 ± 0.08 dex.

Using the recent stellar mass estimates of $\log(M_*/\mathrm{M}_\odot) = 10.55$ by Bresolin et al. (2016), our integrated metallicity for NGC 5236 is displayed as a red star, which can be compared to the metallicity for this same galaxy inferred by Bresolin et al. (2016) shown with a yellow star in Fig. 6. The agreement between these two measurements obtained with independent methods shows the consistency of stellar studies.

A compilation of stellar metallicities obtained using the BSG method along with those using the IL method shows that this 'stellar' MZR is rather similar to the nebular MZR inferred by Andrews & Martini (2013) with an additional scatter and offset towards lower values. We note that the sample size of the stellar metallicity is considerably smaller than the nebular sample. Fig. 6 supports the idea that the correlation between mass and metallicity can, in principle, be studied through the galactic stellar component. However, we point out that a larger measurement sample is needed to draw firmer conclusions.

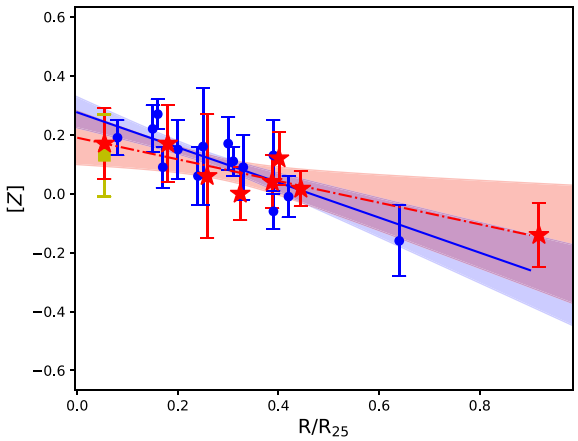

Figure 7. Metallicities as a function of galactocentric distance normalized to isophotal radius. Using red stars we display the YMC metallicity measurements obtained as part of this work. We show the metallicity measurement of Gazak et al. (2014b) for NGC 5236-805 using a yellow square, and using blue circles we show Bresolin et al. (2016) BSG metallicities. Red dashed and blue solid lines display a first-order polynomial fit for YMCs and BSGs, respectively. The salmon (YMCs) and blue (BSGs) shaded regions illustrate the 1σ uncertainties of the linear regressions.

One possible advantage of the stellar over the nebular MZR is the fact that analysis on stellar spectroscopy is more feasible on higher metallicity environments, a regime where measurements become more challenging for H II regions, especially using the direct method (Bresolin et al. 2005; Stasińska 2005; Gazak et al. 2015).

5.2 Comparison to other stellar abundances in NGC 5236

In Fig. 7, we show the metallicities obtained as part of this work (in red stars) as a function of galactocentric distance. The galactocentric distance is normalized to the isophotal radius. This distance, R/R_{25}, is calculated adopting the following parameters: R_{25} = 6.44 arcmin (de Vaucouleurs et al. 1991), i = 24 deg and PA = 45 deg (Comte 1981). We also include the BSG metallicity measurements of Bresolin et al. (2016) for comparison (in blue circles), along with the YMC metallicity from Gazak et al. (2014b) shown as a yellow square.

Before comparing the different metallicity measurements, we homogenize the different sets to a single abundance scale. In this YMC work, we use Grevesse & Sauval (1998) solar composition with a metallicity mass fraction of $Z_{\mathrm{YMC}} = 0.0169$. In contrast, Bresolin et al. use Asplund et al. (2009) solar oxygen abundance and the solar composition of Grevesse & Sauval (1998) for the rest of the elements with a total metallicity mass fraction $Z_{\mathrm{BSG}} = 0.0149$. We scale the BSG metallicities using the following relation:

$$[Z]_{\mathrm{YMC}} = [Z]_{\mathrm{BSG}} - \log\left(\frac{Z_{\mathrm{YMC}}}{Z_{\mathrm{BSG}}}\right) = [Z]_{\mathrm{BSG}} - 0.06. \quad (4)$$

Using the *J*-band spectral analysis method, Gazak et al. (2014b) determined the metallicity of YMC NGC 5236-805, also included in our sample. The authors inferred a metallicity $[Z] = +0.28 \pm 0.14$ dex. We point out that the study of Gazak et al. (2014b) applies a spectral synthesis analysis based on MARCS models, which adopt solar abundances from Grevesse, Asplund & Sauval (2007) and determine the metallicities using several elements such as Fe, Ti, Si and Mg. To account for the difference in solar abundance used in the work of Gazak et al., we revise this value considering the

metallicity mass fraction of Grevesse et al. (2007), $Z_{\rm Jband} = 0.012$, and following the relation:

$$[Z]_{\rm YMC} = [Z]_{\rm Jband} - \log\left(\frac{Z_{\rm YMC}}{Z_{\rm Jband}}\right) = [Z]_{\rm Jband} - 0.15. \quad (5)$$

We revise the metallicity measurement by Gazak et al. to $[Z] = +0.13 \pm 0.14$ dex. With a galactocentric distance of $R/R_{25} \sim 0.05$, NGC 5236-805 is the innermost YMC in our work. We measure an overall metallicity of $[Z] = +0.17 \pm 0.12$ for the same YMC. This value is consistent within the errors with the *J*-band measurement by Gazak et al. (2014b).

To further explore the central stellar metallicity in NGC 5236, we compare our NGC 5236-805 metallicity with that derived by Bresolin et al. (2016) for a BSG with a galactocentric distance of $R/R_{25} \sim 0.08$, relatively close to our central YMC. Bresolin et al. measure a metallicity of $[Z] = +0.25 \pm 0.06$ dex, well within the errors of our inferred value. These three independent measurements, using distinct methods, show excellent agreement, confirming the above-solar metallicity environment in the central regions and inner disc of NGC 5236 and the consistency of stellar metallicities.

From Fig. 7, we can find strong agreement between the metallicities of BSGs and those of the YMCs, especially at $R/R_{25} < 0.5$. In the same figure, we show linear regressions to the YMC metallicities (in red dashed line) and to the BSG metallicities (in blue line). We apply a linear regression only to metallicities with galactocentric distances of $R/R_{25} < 0.5$, obtaining

$$[Z]_{\rm YMC} = -0.37\,(\pm 0.29)\,R/R_{25} + 0.19\,(\pm 0.09) \quad (6)$$

and

$$[Z]_{\rm BSG} = -0.60\,(\pm 0.19)\,R/R_{25} + 0.20\,(\pm 0.05), \quad (7)$$

where $[Z]_{\rm YMC}$ applies to the YMC observations and $[Z]_{\rm BSG}$ to the BSGs. The different slopes inferred through the two methods agree within the errors of each other, with the YMC measurements having a slightly shallower gradient. We point out that gradients of ~ -0.4 dex R_{25}^{-1} are typical for spiral galaxies (Ho et al. 2015). However, the gradient value inferred from the YMCs comes with large uncertainties and a flat distribution with zero gradient is well within 2σ.

Beyond $R/R_{25} \sim 0.5$, both studies have a single metallicity measurement at different radii. In our work, the YMC is at a larger galactocentric distance than the one from Bresolin et al. (2016). Due to the extremely limited number of measurements beyond $R/R_{25} \sim 0.5$, it becomes especially challenging to draw firmer conclusions regarding the spatial distribution of metallicity at larger distances from the centre. Additional metallicity measurements of targets at $R/R_{25} > 0.5$ will help discriminating between an optimal linear fit of a single or multiple gradients.

5.3 Stellar versus gas abundance

The systematic offsets in the inferred metallicities using different nebular diagnostics have been discussed and studied extensively (e.g. Kennicutt et al. 2003; Moustakas et al. 2010; López-Sánchez et al. 2012). In this section, we compare our stellar metallicities to those obtained through the analysis of nebular regions. We take the emission fluxes published by Bresolin et al. (2005) and estimate strong-line abundances applying the O2N2 = [N II] λ6584/[O II] λ3727 method and adopting two different calibrations based on theoretical models and empirical data. We mainly focus on the metallicity characterization of the inner disc ($R/R_{25} < 0.6$) of NGC 5236. We note that there are several other strong-line diagnostics that we have not included here. Bresolin et al. (2016) provide a detailed discussion on strong-line diagnostics along with an extensive comparison to their predicted chemical abundances. The aim of this section is to understand how the stellar metallicities obtained in this work compare to the general trends and values of nebular studies in a general sense and how much our results resemble or differ from those obtained by Bresolin et al. (2016).

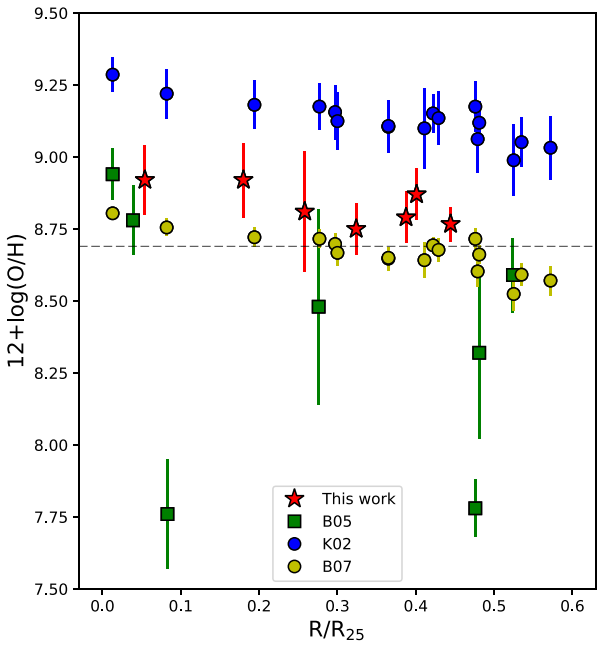

Figure 8. Oxygen abundance as a function of galactocentric distance normalized to the isophotal radius. Using red stars we show the metallicity measurements converted to oxygen abundance inferred in this work. Using blue circles we show the oxygen measurements from the O2N2 calibration by K02. Using yellow circles we show the abundances from B07. Using green squares we show the oxygen abundances inferred from the direct method by B05.

O2N2 – Theoretical: We apply the strong-line calibration for O2N2 by Kewley & Dopita (2002). We refer to this calibration as K02. The method is calibrated using theoretical photoionization models.

O2N2 – Empirical: The O2N2 method by Bresolin (2007) is based on a sample of 140 direct abundance measurements from extragalactic H II regions. We refer to this calibration as B07.

In addition to comparing the metallicities presented in this work to the nebular calibrations above, we also include the abundances obtained by Bresolin et al. (2005) using the direct method. We refer to these measurements as B05. In Fig. 8, we show the oxygen abundances using these four different methods: O2N2/theoretical (K02), O2N2/empirical (B07), direct method (B05) and IL (this work). A visual inspection of this figure shows rather similar slopes for the stellar (in red stars), K02 (in blue circles) and B07 (in yellow circles). On the other hand, Bresolin et al. (2016) find that all the strong-line indicators they investigate, including K02 and B07, have shallower slopes than those measured from the BSG abundances. Considering we find similarities between our slopes and those from K02 and B07, this difference between the gradient by Bresolin et al. (2016) and those from strong-line indicators (K02 and B07) is expected from the inferred gradients for YMCs and BSG shown in equations (6) and (7), where we see that YMCs

point at a shallower slope. Furthermore, a clear offset is present where the oxygen abundances from K02 are higher than our YMC work, by ∼0.3–0.4 dex, and the B07 abundances, by ∼0.5 dex. In this context, these results are similar to those observed in Bresolin et al. (2016) with the BSG abundances lying ∼ 0.2–0.3 dex lower than those calibrated with the K02 method.

The abundances from the direct method, B05, exhibit a rather strong scatter; however, the innermost measurements agree well with our stellar metallicities. We point out that the abundance from B05 of 12 + log(O/H) = 7.75 at R/R_{25} ∼0.08 is merely a lower limit. At $R/R_{25} > 0.2$, the B05 abundances deviate from ours to lower values.

In this comparison, the best agreement between the nebular and stellar abundances is obtained from the empirical B07 calibration, although our measurements are consistently higher than those from the B07 diagnostics. Linear regressions for the B07 data and our measurements show consistent slopes, with our metallicities being offset to higher metallicities by ∼0.1 dex. As pointed out in Bresolin et al. (2016), in these comparisons we do not account for the effect of oxygen depletion (e.g. onto interstellar dust grains). This effect is especially important for oxygen abundances that have been derived from empirical calibrations, such as B07. Mesa-Delgado et al. (2009) and Peimbert & Peimbert (2010) have empirically determined depletion factors ranging between −0.08 and −0.12 dex. Applying an average correction for −0.1 dex of depletion to the B07 nebular abundances brings the measurements to better agreement with our YMC stellar abundances.

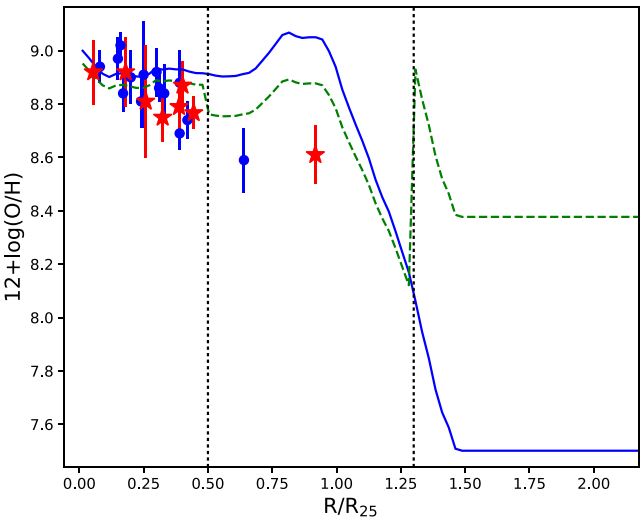

Figure 9. Oxygen abundance as a function of galactocentric distance normalized to isophotal radius. Using red stars we show the YMC measurements inferred in our analysis. Using blue circles we include BSG oxygen abundances from Bresolin et al. (2016). The blue and green dashed lines represent two chemical evolution models for NGC 5236 (Bresolin et al. 2016), accounting for galactic winds (and infall) and closed box, respectively. The dashed vertical lines show the radial divisions used in generating the detailed model.

5.4 Comparison to chemical evolution models

We now compare our direct metallicity measurements with chemical evolution models produced specifically for NGC 5236.

Bresolin et al. (2016) introduced two chemical evolution models for their observed present-day metallicity distribution over the entire NGC 5236 disc. For details on the construction of the different models, we refer the reader to Bresolin et al. (2016). Briefly, their individual models were generated using the analytical chemical evolution model of Kudritzki et al. (2015). This analytical model improves over the closed-box scenario (Pagel & Patchett 1975) by accounting for the influence of gas flows (in and out) to regulate the spatial distribution of abundances. The model of Kudritzki et al. provides theoretical radial metallicity distributions based on specified stellar and gas radial mass profiles with two additional free parameters, infall and outflow. To generate a closed-box model, these two free parameters are set to 0.

In the case of the detailed model involving galactic winds, and in/outfalls, the radial range (R/R_{25}) was divided into three different sections (0.0– 0.5, 0.5–1.3 and 1.3–1.5) where the authors vary the mass flow rates and the infalling gas. The infall and outfall parameters are defined as the ratio of mass infall/outfall rate by the star formation rate, $\dot{M}_{\rm acct}/\psi$ and $\dot{M}_{\rm loss}/\psi$. The best model fit (shown in Fig. 9) required $\dot{M}_{\rm acct}/\psi = 0.0$ and $\dot{M}_{\rm loss}/\psi = 0.12$ for the first section, $\dot{M}_{\rm acct}/\psi = 0.0$ and $\dot{M}_{\rm loss}/\psi = 0.50$ for the second region and $\dot{M}_{\rm acct}/\psi = 1.0$ and $\dot{M}_{\rm loss}/\psi = 0.0$ for the outer disc.

In Fig. 9, we show the detailed (infall+galactic winds) and closed-box chemical models by Bresolin et al. (2016), along with our abundance measurements and those from BSGs. We convert our overall metallicities measured in NGC 5236 adopting a solar oxygen abundance of 12+log(O/H)=9.69 from Asplund et al. (2009). We note that the feature in Fig. 9 in the detailed model (green dashed line) around $R/R_{25} \sim 1.3$ is an artificial spike originating from the two connecting radial sections described above. For distances $R/R_{25} < 0.5$, both models predict relatively similar abundance gradients, although the closed-box model gives slightly higher values.

In general, our observed abundances agree slightly better with the lower oxygen abundances predicted by the detailed model (green dashed line), mainly found in the first radial region where no gas infall is required, and only a small fraction of the material is expelled due to galactic winds. Furthermore, it is clear that for our last abundance measurement at $R/R_{25} = 0.91$, the detailed model predicts a value closer to our oxygen abundance than the closed-box model. Based on this detailed model and our abundance measurement in this second radial region, it appears reasonable to assume a different gradient to describe the metallicity distribution in this region of the disc. However, more stellar metallicity measurements are needed to verify this statement.

5.5 Metallicity–age relation

We observe a clear anticorrelation between the measured metallicities and their corresponding ages. In Fig. 10, we show this relation along with a first-order polynomial fit of the form $[Z] = a\,\log(\text{age}) + b$, represented by a black dashed line. We estimate a slope of $a = -0.24 \pm 0.12$, with a 2σ correlation hinting at a minimum decline in metallicity of ∼0.1 dex in a time period of ∼100 Myr. We note that the oldest YMCs in our sample, NGC 5236-254, has a location $R/R_{25} > 0.5$ and a metallicity lower than the rest by ∼0.15 dex. Similarly, one of the youngest clusters, NGC 5236-805, is the most centrally located and one of the most metal-rich objects in our study. While these observations suggest that the anticorrelation could, in principle, be of a chemical evolution origin, we cannot discard systematic effects in the spectral fitting as a possible cause.

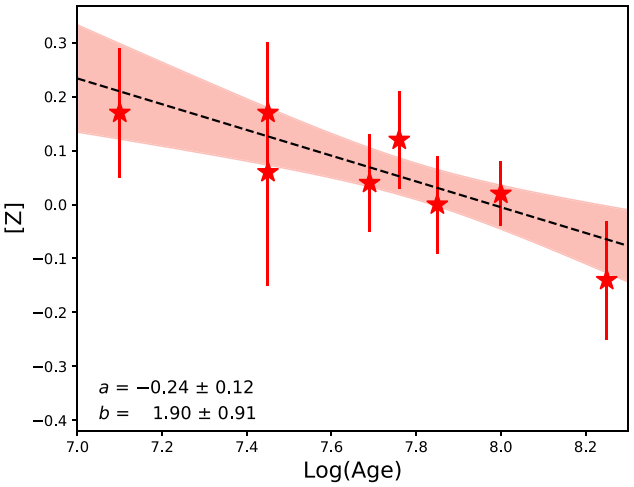

Figure 10. Metallicity as a function of log(age). Using red stars we show the metallicity measurements obtained as part of this work. We show a first-order polynomial fit as a black dashed line. In the shaded salmon region, we show 1σ confidence intervals. We include the slope (a) and zero-point (b) of the linear regression along with their uncertainties.

6 CONCLUSIONS

Chemical abundances of star-forming galaxies, especially beyond the Local Group, are mainly based on the analysis of nebular emission lines. A characteristic problem of nebular studies arises when comparing the abundances obtained through the different calibrators (e.g. O2N2, O3N2, N2) where one can find systematic offsets as high as ∼0.7 dex (Bresolin 2008; Kewley & Ellison 2008). To avoid these poorly understood systematic uncertainties, in this paper we carry out a stellar metallicity analysis on a sample of eight extragalactic YMCs distributed throughout NGC 5236. This stellar abundance approach is of special relevance for environments of metallicities above solar, where certain nebular methods fail or tend to underestimate abundances (Stasińska 2005; Simón-Díaz & Stasińska 2011; Zurita & Bresolin 2012).

We apply the abundance technique developed by L12 for IL observations and show that this can be successfully used on intermediate-resolution spectroscopic data taken with the X-Shooter spectrograph of objects in the high-metallicity range. We derive precise metallicities and find excellent agreement with independent stellar metallicity studies in NGC 5236. We measure a supersolar metallicity of $[Z] = +0.17 \pm 0.12$ dex for the most centrally located YMC NGC 5236-805.

We further compare our abundance measurements to chemical evolution models by Bresolin et al. (2016). Similar to their findings, we observe that their best model, which accounts for galactic winds and in/outflows, reproduces our observed abundances better than their simple closed-box model. Based on this comparison, we conclude that the central regions of NGC 5236 are possibly experiencing no infall of material, and a small loss of material due to galactic winds.

We conclude that the analysis of IL observations is an independent and reliable method for obtaining metallicities and studying galactic abundance gradients in star-forming galaxies in high-metallicity environments. Our results also prove that the X-Shooter spectrograph allows for these types of abundance studies today and expect future instrumentation and telescopes such as the Extremely Large Telescope, the Giant Magellan Telescope and the Thirty Meter Telescope to continue providing essential information on the chemical enrichment of other galaxies. Furthermore, the excellent agreement between two independent methods, IL and BSGs is especially encouraging for future work with these new generation telescopes as an alternative to H II-techniques allowing us to expand our knowledge of galaxy formation and evolution.

ACKNOWLEDGEMENTS

We thank A. Gonneau, Y.-P. Chen and M. Dries for their help and guidance during the X-Shooter reduction process. We are especially thankful to R.-P. Kudritzki for his detailed review of this manuscript, which improved the quality of our work. This research is based on observations made with ESO telescopes at the La Silla Paranal Observatory under programme ID 085.B-0111(A). This research has made use of the NASA/IPAC Extragalactic Database (NED), which is operated by the Jet Propulsion Laboratory, California Institute of Technology, under contract with the National Aeronautics and Space Administration.

REFERENCES

Andrews B. H., Martini P., 2013, ApJ, 765, 140
Asplund M., Grevesse N., Sauval A. J., Scott P., 2009, ARA&A, 47, 481
Bastian N., Cabrera-Ziri I., Davies B., Larsen S. S., 2013, MNRAS, 436, 2852
Bergemann M., Lind K., Collet R., Magic Z., Asplund M., 2012, MNRAS, 427, 27
Bergemann M., Kudritzki R.-P., Gazak Z., Davies B., Plez B., 2015, ApJ, 804, 113
Bernstein R. A., McWilliam A., 2005, in Valls-Gabaud D., Chavez M., eds, ASP Conf. Ser., Resolved Stellar Populations. Astron. Soc. Pac., San Francisco in press (arXiv:astro-ph/0507042)
Bresolin F., 2007, ApJ, 656, 186
Bresolin F., 2008, in Israelian G., Meynet G., eds, The Metal-Rich Universe. Cambridge Univ. Press, Cambridge, p. 155
Bresolin F., Kennicutt J., 2002, ApJ, 572, 838
Bresolin F., Kennicutt R. C., Stetson P. B., 1996, AJ, 112, 1009
Bresolin F., Schaerer D., González Delgado R. M., Stasińska G., 2005, A&A, 441, 981
Bresolin F., Pietrzyński G., Urbaneja M. A., Gieren W., Kudritzki R.-P., Venn K. A., 2006, ApJ, 648, 1007
Bresolin F., Kudritzki R.-P., Urbaneja M. A., Gieren W., Ho I.-T., Pietrzyński G., 2016, ApJ, 830, 64
Bressan A., Marigo P., Girardi L., Salasnich B., Dal Cero C., Rubele S., Nanni A., 2012, MNRAS, 427, 127
Chen Y., Trager S. C., Peletier R. F., Lançon A., Vazdekis A., Prugniel P., Silva D. R., Gonneau A., 2014, A&A, 565, A117
Colucci J. E., Bernstein R. A., Cameron S., McWilliam A., Cohen J. G., 2009, ApJ, 704, 385
Colucci J. E., Bernstein R. A., Cameron S. A., McWilliam A., 2011, ApJ, 735, 55
Colucci J. E., Bernstein R. A., Cameron S. A., McWilliam A., 2012, ApJ, 746, 29
Comte G., 1981, A&AS, 44, 441
Davies B., Kudritzki R., Figer D. F., 2010, MNRAS, 407, 1203
de Vaucouleurs G., de Vaucouleurs A., Corwin H. G. Jr, Buta R. J., Paturel G., Fouqué P., 1991, Third Reference Catalogue of Bright Galaxies. Springer-Verlag, Berlin
Ercolano B., Wesson R., Bastian N., 2010, MNRAS, 401, 1375
Evans C. J., Bresolin F., Urbaneja M. A., Pietrzyński G., Gieren W., Kudritzki R.-P., 2007, ApJ, 659, 1198
Finlator K., Davé R., 2008, MNRAS, 385, 2181
Gazak J. Z. et al., 2014a, ApJ, 787, 142
Gazak J. Z., Davies B., Kudritzki R., Bergemann M., Plez B., 2014b, ApJ, 788, 58
Gazak J. Z. et al., 2015, ApJ, 805, 182

Girardi L., Chiosi C., Bertelli G., Bressan A., 1995, A&A, 298, 87
Grevesse N., Sauval A. J., 1998, Space Sci. Rev., 85, 161
Grevesse N., Asplund M., Sauval A. J., 2007, Space Sci. Rev., 130, 105
Gustafsson B., Edvardsson B., Eriksson K., Jørgensen U. G., Nordlund Å., Plez B., 2008, A&A, 486, 951
Hernandez S., Larsen S., Trager S., Groot P., Kaper L., 2017, A&A, 603, A119
Ho I.-T., Kudritzki R.-P., Kewley L. J., Zahid H. J., Dopita M. A., Bresolin F., Rupke D. S. N., 2015, MNRAS, 448, 2030
Hosek M. W., Jr et al., 2014, ApJ, 785, 151
Jacobs B. A., Rizzi L., Tully R. B., Shaya E. J., Makarov D. I., Makarova L., 2009, AJ, 138, 332
Kennicutt R. C., Jr et al., 2003, PASP, 115, 928
Kewley L. J., Dopita M. A., 2002, ApJS, 142, 35
Kewley L. J., Ellison S. L., 2008, ApJ, 681, 1183
Kudritzki R.-P., Urbaneja M. A., Gazak Z., Bresolin F., Przybilla N., Gieren W., Pietrzyński G., 2012, ApJ, 747, 15
Kudritzki R.-P., Urbaneja M. A., Gazak Z., Macri L., Hosek M. W., Jr, Bresolin F., Przybilla N., 2013, ApJ, 779, L20
Kudritzki R.-P., Urbaneja M. A., Bresolin F., Hosek M. W., Jr, Przybilla N., 2014, ApJ, 788, 56
Kudritzki R.-P., Ho I.-T., Schruba A., Burkert A., Zahid H. J., Bresolin F., Dima G. I., 2015, MNRAS, 450, 342
Kudritzki R. P., Castro N., Urbaneja M. A., Ho I.-T., Bresolin F., Gieren W., Pietrzyński G., Przybilla N., 2016, ApJ, 829, 70
Kurucz R. L., 1970, SAO Special Report #309
Kurucz R. L., Avrett E. H., 1981, SAO Special Report #391
Kurucz R. L., Furenlid I., 1979, SAO Special Report #387
Lardo C., Davies B., Kudritzki R.-P., Gazak J. Z., Evans C. J., Patrick L. R., Bergemann M., Plez B., 2015, ApJ, 812, 160
Larsen S. S., 1999, A&A, 139, 393
Larsen S. S., 2004, A&A, 415, 537
Larsen S. S., 2009, A&A, 494, 539
Larsen S. S., Richtler T., 1999, A&A, 345, 59
Larsen S. S., Richtler T., 2004, A&A, 427, 495
Larsen S. S., Richtler T., 2006, A&A, 459, 103
Larsen S. et al., 2011, A&A, 532, A147
Larsen S. S., Brodie J. P., Strader J., 2012, A&A, 546, A53 (L12)
Larsen S. S., Brodie J. P., Forbes D. A., Strader J., 2014, A&A, 565, A98
Lee J. C., Salzer J. J., Melbourne J., 2004, ApJ, 616, 752
Lequeux J., Peimbert M., Rayo J. F., Serrano A., Torres-Peimbert S., 1979, A&A, 80, 155
Lilly S. J., Carollo C. M., Pipino A., Renzini A., Peng Y., 2013, ApJ, 772, 119
López-Sánchez, Á. R., Dopita M. A., Kewley L. J., Zahid H. J., Nicholls D. C., Scharwächter J., 2012, MNRAS, 426, 2630
Lyubimkov L. S., Rostopchin S. I., Lambert D. L., 2004, A&A, 351, 745
McWilliam A., Bernstein R. A., 2002, in Geisler D., Grebel E. K., Minniti D., eds, Proc. IAU Symp. 207, Extragalactic Star Clusters. Astron. Soc. Pac., San Francisco, p. 739
McWilliam A., Bernstein R. A., 2008, ApJ, 684, 326
Maiolino R. et al., 2008, A&A, 488, 463
Matteucci F., 2003, Ap&SS, 284, 539
Mesa-Delgado A., Esteban C., García-Rojas J., Luridiana V., Bautista M., Rodríguez M., López-Martín L., Peimbert M., 2009, MNRAS, 395, 855
Moustakas J., Kennicutt R. C., Jr, 2006, ApJ, 651, 155
Moustakas J., Kennicutt R. C., Jr, Tremonti C. A., Dale D. A., Smith J.-D. T., Calzetti D., 2010, ApJS, 190, 233
Pagel B. E. J., Patchett B. E., 1975, MNRAS, 172, 13
Pagel B. E. J., Edmunds M. G., Blackwell D. E., Chun M. S., Smith G., 1979, MNRAS, 189, 95
Peimbert A., Peimbert M., 2010, ApJ, 724, 791
Plez B., 2012, Astrophysics Source Code Library, record ascl:1205.004
Portegies Zwart S. F., McMillan S. L. W., Gieles M., 2010, ARA&A, 48, 431
Prantzos N., Boissier S., 2000, MNRAS, 313, 338
Pritzl B. J., Venn K. A., Irwin M., 2005, AJ, 130, 2140
Rubin R. H., Simpson J. P., Lord S. D., Colgan S. W. J., Erickson E. F., Haas M. R., 1994, ApJ, 420, 772
Salpeter E. E., 1955, ApJ, 121, 161
Sánchez-Blázquez P., Courty S., Gibson B. K., Brook C. B., 2009, MNRAS, 398, 591
Simón-Díaz S., Stasińska G., 2011, A&A, 526, A48
Stasińska G., 2005, A&A, 434, 507
Tremonti C. A. et al., 2004, ApJ, 613, 898
Venn K. A., Irwin M., Shetrone M. D., Tout C. A., Hill V., Tolstoy E., 2004, AJ, 128, 1177
Vernet J. et al., 2011, A&A, 536A, 105
Worthey G., 1998, PASP, 110, 888
Zaritsky D., Kennicutt R. C., Jr, Huchra J. P., 1994, ApJ, 420, 87
Zurita A., Bresolin F., 2012, MNRAS, 427, 1463

APPENDIX: METALLICITIES AS A FUNCTION OF WAVELENGTH

We present tables displaying the individual bin measurements for each of the YMCs studied in this work.

Table A1. Metallicities for NGC 5236-245.

Wavelength (Å)	[*Z*]	Error
4000–4200	+0.043	0.265
4200–4400	+0.236	0.454
6100–6300	−0.374	0.129
6300–6500	+0.199	0.127
6588–6700	+0.069	0.129
6700–6800	−0.183	0.192
7400–7550	+0.003	0.093
8500–8700	+0.034	0.065
8700–8830	+0.129	0.102

Table A2. Metallicities for NGC 5236-254.

Wavelength (Å)	[*Z*]	Error
4000–4200	+0.133	0.134
4200–4400	+0.133	0.104
6100–6300	+0.153	0.087
6300–6500	−0.175	0.136
6588–6700	−0.502	0.175
6700–6800	−0.573	0.242
7400–7550	+0.369	0.100
8500–8700	−0.305	0.043
8700–8830	−0.400	0.104

Table A3. Metallicities for NGC 5236-367.

Wavelength (Å)	[*Z*]	Error
4000–4200	−0.641	0.129
4200–4400	−0.271	0.132
6100–6300	−0.175	0.071
6300–6500	+0.199	0.074
6588–6700	−0.008	0.112
6700–6800	−0.180	0.159
7400–7550	+0.159	0.075
8500–8700	−0.192	0.130
8700–8830	+0.269	0.081

Table A4. Metallicities for NGC 5236-805.

Wavelength (Å)	[Z]	Error
4000–4200	+0.361	0.033
4200–4400	+0.026	0.047
6100–6300	+0.039	0.027
6300–6500	+0.090	0.033
6588–6700	+0.155	0.029
6700–6800	−0.116	0.053
7400–7550	−0.284	0.126
8500–8700	+0.951	0.113
8700–8830	+0.292	0.024

Table A5. Metallicities for NGC 5236-1182.

Wavelength (Å)	[Z]	Error
4000–4200	+0.302	0.047
4200–4400	+0.312	0.035
6100–6300	+0.406	0.043
6300–6500	−0.344	0.065
6588–6700	−0.446	0.051
6700–6800	−0.548	0.073
7400–7550	+0.188	0.026
8500–8700	−0.426	0.108
8700–8830	+0.251	0.021

Table A6. Metallicities for NGC 5236-1234.

Wavelength (Å)	[Z]	Error
4000–4200	−0.034	0.104
4200–4400	−0.764	0.149
6100–6300	−0.938	0.171
6300–6500	−0.816	0.109
6588–6700	+0.863	0.096
6700–6800	+0.053	1.038
7400–7550	+0.263	0.055
8500–8700	−0.732	0.132
8700–8830	+0.177	0.053

Table A7. Metallicities for NGC 5236-1389.

Wavelength (Å)	[Z]	Error
4000–4200	−0.197	0.083
4200–4400	−0.506	0.073
6100–6300	−0.342	0.165
6300–6500	−0.003	0.066
6588–6700	+0.008	0.140
6700–6800	+0.064	0.103
7400–7550	+0.310	0.052
8500–8700	−0.400	0.125
8700–8830	+0.228	0.048

Table A8. Metallicities for NGC 5236-1471.

Wavelength (Å)	[Z]	Error
4000–4200	−0.331	0.124
4200–4400	+0.342	0.091
6100–6300	+0.016	0.108
6300–6500	+0.246	0.100
6588–6700	+0.326	0.204
6700–6800	+0.008	0.142
7400–7550	+0.256	0.061
8500–8700	−0.082	0.032
8700–8830	+0.568	0.050

This paper has been typeset from a TEX/LATEX file prepared by the author.